JTTEE5 21:1245–1256
DOI: 10.1007/s11666-012-9825-3
1059-9630/$19.00 © ASM International

Influence of Bond Coats on the Microstructure and Mechanical Behaviors of HVOF-Deposited TiAlNb Coatings

H.J. Zeng, L.Q. Zhang, J.P. Lin, X.Y. He, Y.C. Zhang, and P. Jia

(Submitted March 31, 2012; in revised form September 15, 2012)

Hot dip galvanizing has been extensively employed for corrosion protection of steel structures. However, during the process of galvanization, the corrosion in molten zinc brings many problems to galvanization industry. In this study, as a material of corrosion resistance to molten zinc intended for application in Hot-dip galvanization, HVOF $Ti_{28.15}Al_{63.4}Nb_{8.25}Y$ (at.%) coatings with different bond coats (NiCr5Al, NiCoCrAlY, CoCrAlYTaSi, and NiCr80/20) were deposited onto 316L stainless steel substrate, respectively. The influences of different bond coats on HVOF $Ti_{28.15}Al_{63.4}Nb_{8.25}Y$ coatings were investigated. The results showed that bond coat had an obvious influence on improving the mechanical properties of HVOF $Ti_{28.15}Al_{63.4}Nb_{8.25}Y$ coatings. HVOF $Ti_{28.15}Al_{63.4}Nb_{8.25}Y$ coatings with NiCoCrAlY bond coat displayed the best mechanical properties. However, bond coats had no obvious effects on the microstructure, porosity, and hardness of HVOF $Ti_{28.15}Al_{63.4}Nb_{8.25}Y$ top coatings. The effects of as-received powder morphology and grain size on the characteristics of coatings were also discussed.

Keywords bond strength, high velocity oxygen-fuel, porosity, thermal shock test, TiAlNb intermetallic compound

1. Introduction

Hot-dip galvanization is one of the best and most extensively employed methods to protect steel against corrosion (Ref 1-5). However, there is a critical problem of almost all components of galvanizing equipment being corroded by molten zinc at temperatures 460-650 °C in the galvanization process. The formation of intermetallic phases and alloys developed on the surface of galvanized components during galvanization brings a series of problems to galvanization industry (Ref 2, 6).

In a continuous galvanizing line (CGL), the bath hardware such as pot roll is very important because it is in direct contact with the liquid zinc. Stainless steels are generally used as roll materials, but their corrosion resistance to molten zinc is not good enough (Ref 7). To improve the surface characteristics of materials, different types of thermal spray processes can be used (Ref 8-10). HVOF spray process is an economical and effective thermal spray process to deposit more dense and less oxidized coating than air plasma spraying (Ref 11-13).

HVOF WC-Co coating on 316L stainless steel is used in the CGL (Ref 14-17). But the lifetime of HVOF WC-Co coating in molten zinc is approximately 2 weeks. An improvement in the material used for the bath hardware in hot-dip galvanizing would mean a decrease in the frequency of line shutdowns and expensive bath hardware changes.

The major requirement for any coating is to establish an adhesion pattern to the substrate that permits to maintain its integrity under service conditions (Ref 18). Debonding of the top layer or of the bond coat layer will lead to the collapse of the overall coating system. Several possible factors such as residual stresses, pores, cracks, bond strength, and thermal shock property will affect the coating structural integrity (Ref 19–22).

Recently, a novel thermal spray material of MoB/CoCr with higher durability in molten Al-Zn alloys has been developed (Ref 15, 23). The lifetimes of HVOF MoB/CoCr coatings (>600 h) show dramatically longer operating lifetimes when compared to conventional HVOF WC-Co and WC-Co-Cr coatings in molten alloys of Al-45 wt.% Zn and 55 wt.% Al-Zn-1.5 wt.% Si (Ref 15, 24). From the work we carried out, we found that TiAlNb alloys (such as $Ti_4Nb_3Al_9$ (at.%) and $TiAl_{45}Nb_8$ (at.%) alloys) in bulk form had excellent corrosion resistance to molten zinc in molten alloy of Zn-0.2 wt.% Al (Ref 7, 25, 26). The lifetime of $Ti_4Nb_3Al_9$ (at.%) alloy in molten zinc exceeded 150 days. But, they cannot be employed as integral workpiece due to their brittleness. The HVOF $Ti_4Nb_3Al_9$ (at.%) and $Ti_{28.15}Al_{63.4}Nb_{8.25}Y$ (at.%) coatings in the previous works also showed good corrosion resistance to molten zinc. The lifetime of HVOF $Ti_4Nb_3Al_9$

H.J. Zeng, L.Q. Zhang, J.P. Lin, and **X.Y. He**, State Key Laboratory for Advanced Metals and Materials, University of Science and Technology Beijing, Beijing 100083, People's Republic of China; and **Y.C. Zhang** and **P. Jia**, Beijing Langqiao Surface Technology Co., Ltd., Beijing 100089, People's Republic of China. Contact e-mails: pepsi.100@163.com and zhanglq@ustb.edu.cn

coatings reached 45 days and HVOF $Ti_{28.15}Al_{63.4}Nb_{8.25}Y$ coatings kept integrity after a long time in molten zinc. To improve the lifetime of immersed bath hardware in continuous hot-dip galvanizing line, the TiAlNb intermetallic compounds are potentially suitable materials for application in the galvanizing industry.

To enhance the lifetime of HVOF TiAlNb coating, the effects of spraying parameters on the coatings have been discussed (Ref 27). In this study, four different kinds of bond coat materials (NiCr5Al, NiCoCrAlY, CoCrAlYTaSi, and NiCr80/20) were deposited onto 316L stainless steel using HVOF thermal spraying. The preparation of $Ti_{28.15}Al_{63.4}Nb_{8.25}Y$ powder was easier than that of $Ti_4Nb_3Al_9$ alloy due to its brittleness, so, the $Ti_{28.15}Al_{63.4}Nb_{8.25}Y$ intermetallic compound of good oxidation resistance was selected to serve as top coat material. The influence of bond coats on bond strength, microstructure, hardness, porosity, and thermal shock property of HVOF $Ti_{28.15}Al_{63.4}Nb_{8.25}Y$ top coating was investigated. In this study, we attempted to select a kind of bond coat material suitable for HVOF $Ti_{28.15}Al_{63.4}Nb_{8.25}Y$ top coating and to improve the mechanical behaviors of HVOF $Ti_{28.15}Al_{63.4}Nb_{8.25}Y$ coating.

2. Experimental Procedures

2.1 Powder and Specimen Preparation

The top coat material of $Ti_{28.15}Al_{63.4}Nb_{8.25}Y$ (at.%) alloy was prepared from high-purity titanium chip (99.99 wt.%), aluminum (99.99 wt.%), yttrium (99.9 wt.%), and Nb-Al master alloy (99.9 wt.%, Nb74.48 wt.%, and Al25.52 wt.%) by arc-melting using a nonconsumable electrode under high-purity argon. To ensure compositional uniformity, each button was melted for five times. The $Ti_{28.15}Al_{63.4}Nb_{8.25}Y$ (at.%) powder was prepared by shake crusher (J100-I, Nanchang, China). First, the $Ti_{28.15}Al_{63.4}Nb_{8.25}Y$ (at.%) alloy was crushed to small pieces with the diameter of <5 mm. Then the small pieces of $Ti_{28.15}Al_{63.4}Nb_{8.25}Y$ (at.%) alloy were put in shake crusher and mechanical crushed once in 1 min. Powder was achieved by sieving using the sieve of 350 mesh before spraying in accordance with the projection characteristics of HVOF spraying system. Four kinds of commercially available powders offered by Beijing General Research Institute of Mining and Metallurgy were used as bond coat materials. The commercial names of the four powders employed are KF-110 (NiCr5Al), KF-113 (NiCoCrAlY), KF-330 (CoCrAlYTaSi), and KF-306 (NiCr80/20). The morphology and characterization of the as-received powders are shown in Fig. 1 and Table 1, respectively. The powders display nonspherical or spherical morphology, as shown in Fig. 1.

Laser grain size distribution analysis apparatus (LMS-30, Japan) was applied for grain size distribution test of $Ti_{28.15}Al_{63.4}Nb_{8.25}Y$ powder. The medium size (D_{50}) of powder is 15.5 μm, as shown in Table 1. The 316L steel with the composition of 0.03 wt.% C, 0.08 wt.% Mn, 0.035 wt.% P, 0.025 wt.% S, 10.25 wt.% Ni, 18.0 wt.% Cr, and 2 wt.% Mo was used as a substrate because of its industrial application to rolls. Prior to deposition, the substrate was grit blasted using brown corundum of 24 mesh with the blasting pressure of 0.42 MPa. The roughness Ra is 8.33 μm measured by (TR-240, Beijing Times, China) roughness analysis apparatus (Ref 27). The thermal expansion coefficient was obtained by thermal expansion analysis apparatus (NETZSCH DIL 402C, Germany). The sample was measured under high-purity argon with the dimensions of ∅5 × 25 mm.

2.2 Deposition of HVOF Coatings

HVOF spraying was carried out using DJ-2700 with a DJ9W/DJM spray gun (Sulzer Metco AG, Switzerland). The oxygen to fuel (Propane) ratio was 5.5 during the spraying process of HVOF $Ti_{28.15}Al_{63.4}Nb_{8.25}Y$ top coating and it corresponded to a slight oxygen-rich mixture. Oxygen and fuel reacted in the mixing zone of the spray gun and the stream accelerated the powder to supersonic speed. The materials were sprayed onto 50 × 50 × 6 mm 316L stainless steel for sample characterization and ∅25.4 × 50 mm steel cylinders for the tensile adhesion tests. Air jet was used as cooling media, directed to the surface of the coating, to keep the surface temperature below 150 °C during the spraying process. The infrared temperature measurement apparatus was applied in surface temperature measurement of sprayed coatings. The spraying parameters of HVOF $Ti_{28.15}Al_{63.4}Nb_{8.25}Y$ coatings are shown in Table 2. During the HVOF spraying process of bond coats and $Ti_{28.15}Al_{63.4}Nb_{8.25}Y$ top coats, the spraying pressures of air, oxygen, and fuel (propane) are 0.69, 1.03, and 0.76 MPa, respectively. The bond coat and top coat thicknesses were fixed as $d = 150 \pm 20$ μm, respectively. The total number of torch cycles for different bond coats (NiCr5Al, NiCoCrAlY, CoCrAlYTaSi, and NiCr80/20) and $Ti_{28.15}Al_{63.4}Nb_{8.25}Y$ top coats is 10 and 15, respectively.

2.3 Bond Strength Test

The tensile adhesion test specified by ASTM C633-01 (Ref 28) was used to measure the tensile bonding strength of coating. In performing this test, two identical cylindrical rods (∅25.4 × 50 mm), one with coating on the flat surface and the other without coating, were prepared. The flat surface of the uncoated rod, which was to be bonded to the coated rod, was sand-blast-roughened to enhance resin adherence. The schematic illustration of tensile adhesion test is shown in Fig. 2. A thin layer of E-7 adhesive glue with a tensile fracture strength of over 70 MPa was applied. After the two rods were aligned, the compressive stress was applied to both rods to assure intimate contact between the resin and the two surfaces. After 1 h of drying at 149 °C, the bonded rods were cooled to room temperature. The tensile bonding strength was measured by a material tester (100 kN load cell; Shenzhen, China) at a cross-head speed of 1 mm/min. The value achieved represented an average of five tests.

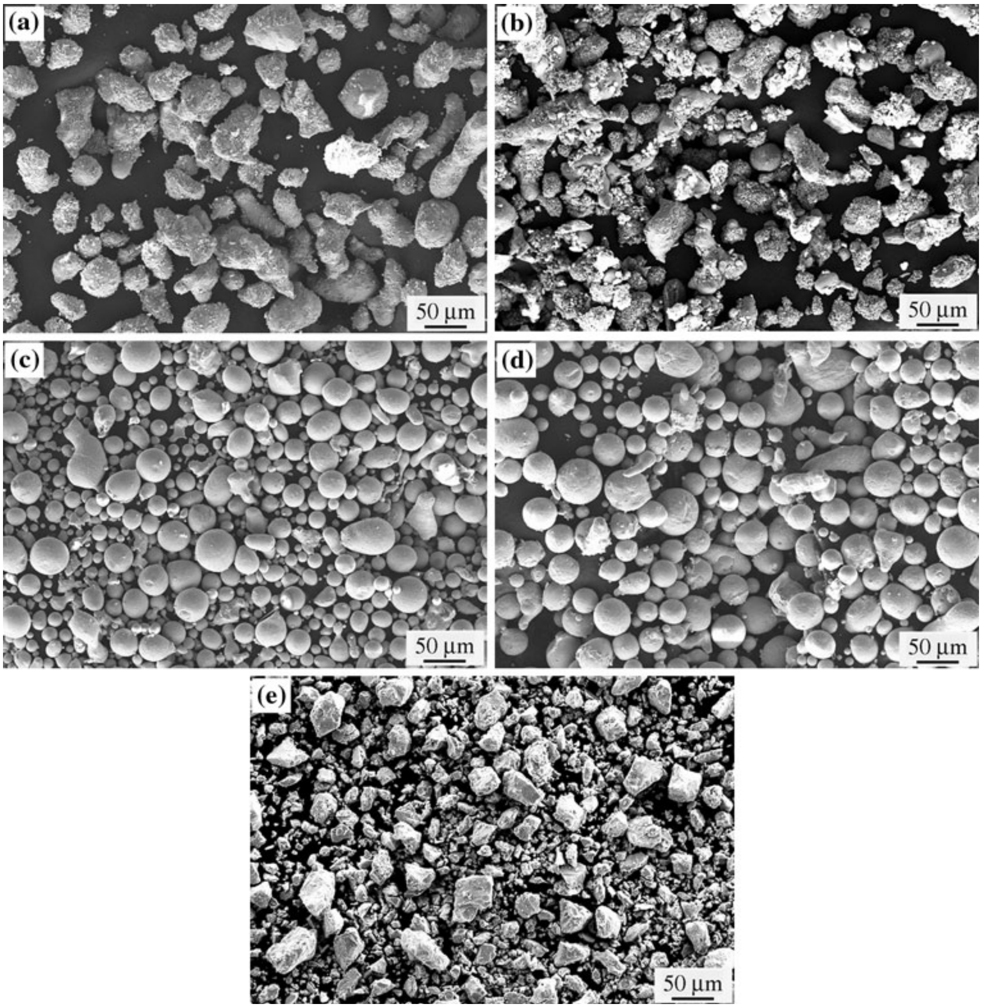

Fig. 1 SEM morphologies of as-received (a) NiCr5Al, (b) NiCoCrAlY, (c) NiCr80/20, (d) CoCrAlYTaSi, and (e) $Ti_{28.15}Al_{63.4}Nb_{8.25}Y$ powders

Table 1 Characterization of as-received powder

	Composition, at.%										
Powder	**Ti**	**Al**	**Nb**	**Y**	**Ni**	**Cr**	**Co**	**Ta**	**Si**	**Particle size, μm**	**Morphology**
$Ti_{28.15}Al_{63.4}Nb_{8.25}Y$	26.79	65.49	7.52	0.19	…	…	…	…	…	$D_{10} = 5.9 D_{50} = 15.5 D_{90} = 33.2$	Nonspherical
NiCr5Al	…	11.94	…	…	69.49	18.57	…	…	…	$D_{10} = 7.3 D_{50} = 22.3 D_{90} = 41.7$	Nonspherical
NiCoCrAlY	…	17.71	…	0.51	41.65	20.03	20.1	…	…	$D_{10} = 8.2 D_{50} = 24.1 D_{90} = 43.6$	Nonspherical
NiCr80/20	…	…	…	…	77.23	22.77	…	…	…	$D_{10} = 19.8 D_{50} = 33.1 D_{90} = 52.3$	Spherical
CoCrAlYTaSi	…	18.61	…	1.69	…	27.44	44.38	1.42	5.32	$D_{10} = 26.3 D_{50} = 39.4 D_{90} = 58.6$	Spherical

Table 2 Spraying parameters of HVOF $Ti_{28.15}Al_{63.4}Nb_{8.25}Y$ coatings

Coating tape	**Flow of air, L/min**	**Flow of oxygen, L/min**	**Flow of propane, L/min**	**Spray distance, mm**	**Movement speed of spraying gun, mm/s**	**Powder feed rate, g/min**
$Ti_{28.15}Al_{63.4}Nb_{8.25}Y$	372.8	143.1	26.4	200	700	10
NiCr5Al	357.9	197.6	26.4	200	700	30
NiCoCrAlY	357.9	197.6	26.4	200	700	30
CoCrAlYTaSi	357.9	197.6	26.4	200	700	30
NiCr80/20	357.9	197.6	26.4	200	700	30

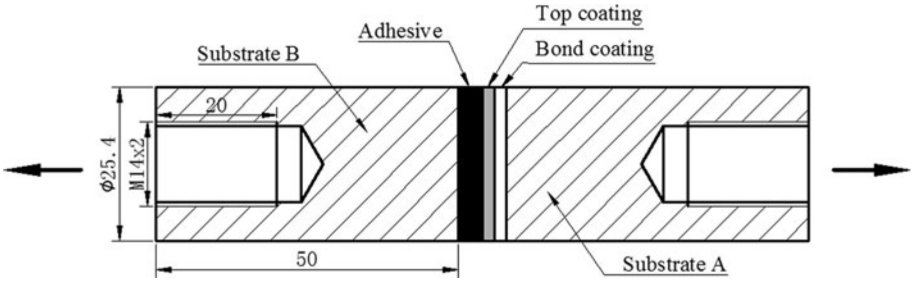

Fig. 2 Schematic illustration of the ‘‘tensile adhesion’’ test apparatus

2.4 XRD and Morphology Analysis

Thermal sprayed (HVOF) coatings with dimensions of 10 × 8 × 6 mm were used for the microstructure, porosity, and hardness analyses. Before testing, the samples were mounted in bakelite and ground using SiC paper down to 2000 #. After they were ground with SiC paper, bakelite-mounted samples were polished and then ultrasonically cleaned using acetone and deionized water for 10 min in turn. The cross-sectional morphology of coating was observed by scanning electron microscopy (SEM) with energy-dispersive x-ray spectrometry (EDX). Before the samples were bakelite-mounted, x-ray diffraction (D/Mar-rB, Rigaku, Japan) using Cu Kα radiation was used to measure the phase of the bond coats (NiCr5Al, NiCoCrAlY, CoCrAlYTaSi, and NiCr80/20) and the HVOF $Ti_{28.15}Al_{63.4}Nb_{8.25}Y$ top coatings.

2.5 Porosity Test

Porosity was determined by the photoshop and image tool (UTHSCSA) analysis. The porosity was measured on the cross section of the samples. Optical image analysis was used to determine the area percentage of open and connected pores to determine the porosity. The porosity value of every coating was the average of ten measurements and the optical micrographs used were at 2500× magnification.

2.6 Microhardness Test

Vickers hardness tests were conducted with a 100 g load and a dwell time of 15 s using a computer image analysis system. The indent dimensions were set manually. The cross section metallographic samples with coating prepared for SEM analysis were used to measure the microhardness. Hardness for each component-substrate, bond coat, and top coat of the HVOF $Ti_{28.15}Al_{63.4}Nb_{8.25}Y$ coatings with different bond coats was measured using the Vickers hardness tests. A through-thickness evolution of hardness in each coating system was scrutinized from the substrate to the HVOF $Ti_{28.15}Al_{63.4}Nb_{8.25}Y$ top coating. Hardness value of each data point mentioned in experimental results is an average of ten indents.

2.7 Thermal Shock Test

The thermal shock test was performed by water quenching method. The samples with dimensions of 50 × 50 × 6 mm were heated in SX_2-2.5-12 box furnace in air for 20 min at 600 °C and then quenched into water at a temperature of 25 °C. Spallation with more than 20% of the total area of the top coat was adopted as the criteria for coating failure. The number of thermal cycles was recorded and was the average of three measurements for every kind of sample.

3. Results and Discussion

3.1 Microstructure of the Coating

Figure 3 showed the typical morphologies of HVOF $Ti_{28.15}Al_{63.4}Nb_{8.25}Y$ coatings with different bond coats (NiCr5Al, NiCoCrAlY, CoCrAlYTaSi, and NiCr80/20). The coatings (Fig. 3a to d) displayed a lamellar structure. Figure 3 exhibited the limited porosity and partially melted particles in bond coats; and further, there are gaps or pores existed in the interface between bond coat and substrate. The unmelted particles of bond coats resulted in the appearing of gaps or pores in the interface between bond coat and substrate. The adhesive strength, hardness, and thermal shock resistance of the whole HVOF $Ti_{28.15}Al_{63.4}Nb_{8.25}Y$ coatings decreased due to the increase of the defects, such as pores and oxides. The compact microstructure between the coating and the substrate is beneficial to the improvement of adhesive strength (Ref 29).

High-magnification (5000×) SEM micrograph of the HVOF $Ti_{28.15}Al_{63.4}Nb_{8.25}Y$ coating is shown in Fig. 4. EDS analysis was employed to analyze the possible phases in the HVOF $Ti_{28.15}Al_{63.4}Nb_{8.25}Y$ coating. The analyses were carried out on the typical points marked as points a-c. Table 3 shows the EDS results obtained for those points. It was clear that point a was the unmelted $Ti_{28.15}Al_{63.4}Nb_{8.25}Y$ powder. The white area of point b was the Niobium-rich phase. Slight amount of oxide inclusions was detected at the grain boundary as shown by point c. The percentage of oxide inclusions in the HVOF $Ti_{28.15}Al_{63.4}Nb_{8.25}Y$ top coatings and bond coats (NiCr5Al, NiCoCrAlY, CoCrAlYTaSi, and NiCr80/20) was <0.3 and $<0.5\%$, respectively, which were measured by image tool (UTHSCSA) software.

The $Ti_{28.15}Al_{63.4}Nb_{8.25}Y$ powder particles melted more extensively than the bond coat powder particles, on account of their finer particle size and lower melting point

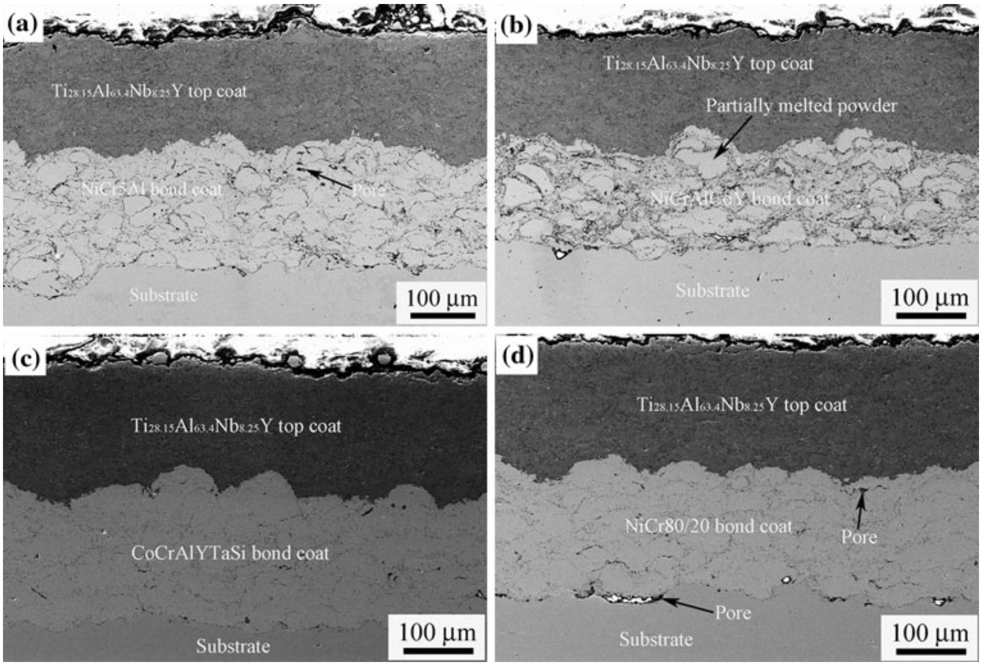

Fig. 3 Typical cross-sectional morphologies of the HVOF $Ti_{28.15}Al_{63.4}Nb_{8.25}Y$ coatings with 316L stainless steel substrate and different bond coat materials. (a) NiCr5Al, (b) NiCoCrAlY, (c) CoCrAlYTaSi, and (d) NiCr80/20 bond coat

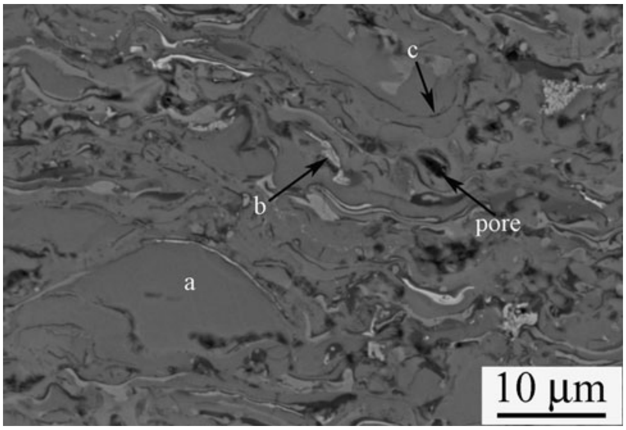

Fig. 4 High-magnification SEM micrograph of the HVOF $Ti_{28.15}Al_{63.4}Nb_{8.25}Y$ coating

Table 3 EDS results of the marked points on the HVOF $Ti_{28.15}Al_{63.4}Nb_{8.25}Y$ coating in Fig. 4

EDS points	Ti, at.%	Al, at.%	Nb, at.%	Y, at.%	O, at.%
a	27.35	63.47	9.03	0.15	…
b	12.07	23.0	64.93	…	…
c	18.61	25.32	5.76	…	50.31

(approximately 1400 °C). The relatively low amount of unmelted inclusions in the top coat would be the main reason for the high density of the top coat. Furthermore, the localized plastic deformation of bond coat impinging particles upon impact was insufficient, thus resulting in the formation of small voids between two adjacent particles (Ref 30). So, the top coats had denser and more compact microstructures than bond coats.

3.2 XRD Analysis

X-ray diffraction patterns for the bond coats (NiCr5Al, NiCoCrAlY, CoCrAlYTaSi, and NiCr80/20) and HVOF $Ti_{28.15}Al_{63.4}Nb_{8.25}Y$ top coat were shown in Fig. 5. A melting with rapid solidification process would rather lead to the formation of metastable super-saturated solid solutions. The XRD analysis of bond coats revealed that the HVOF NiCr5Al bond coating included γ-Ni and γ′-Ni_3Al phases; the HVOF NiCoCrAlY bond coating contained γ-Ni, γ-Co, γ-Cr, and γ′-Ni_3Al phases; the HVOF CoCrAlYTaSi bond coating was composed of γ-Co, γ-Cr, and β-AlCo phases; the HVOF NiCr80/20 bond coating mainly consisted of γ-Ni and γ-Cr phases. The result is in according with findings published in a previous study (Ref 31).

As revealed by Fig. 5, The HVOF $Ti_{28.15}Al_{63.4}Nb_{8.25}Y$ top coat was composed of γ-TiAl, $TiAl_2$, and $AlTi_3$ phases. Previous studies done by Zeng et al. (Ref 27) revealed that the starting powder mainly consisted of γ-TiAl and $TiAl_2$ phases. This suggests that a new $AlTi_3$ phase is presented in the HVOF $Ti_{28.15}Al_{63.4}Nb_{8.25}Y$ top coat. The deposited spray particles have reached melting state prior to the impact on substrate. After having been sprayed, the powder cooled rapidly to the room temperature. The high cooling rate induced the formation of $AlTi_3$ metastable phase.

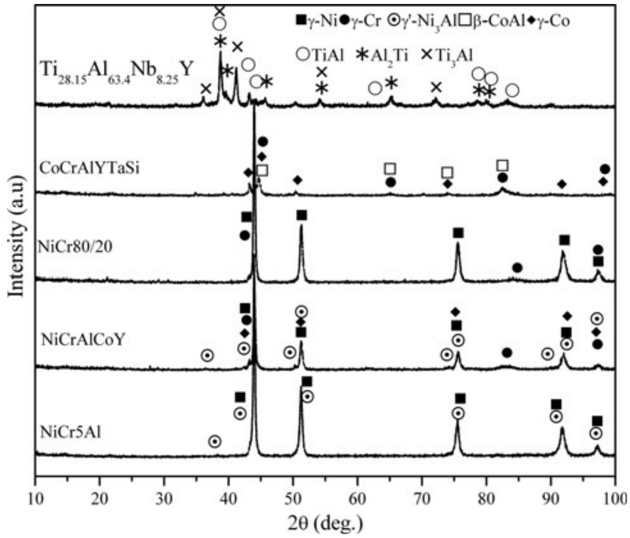

Fig. 5 XRD patterns of HVOF $Ti_{28.15}Al_{63.4}Nb_{8.25}Y$ top coat and the bond coats of NiCr5Al, NiCoCrAlY, CoCrAlYTaSi, and NiCr80/20

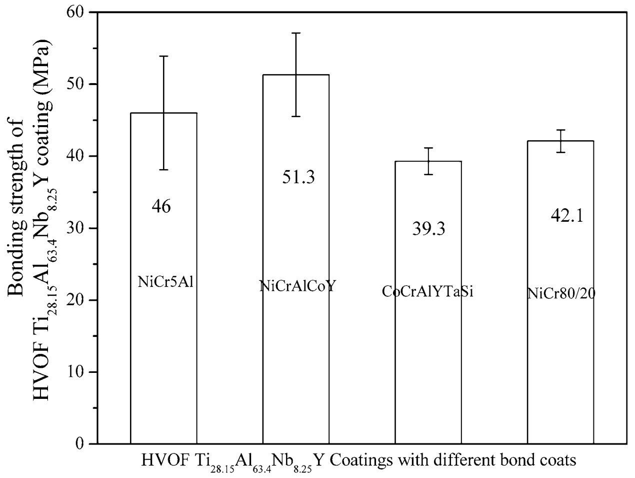

Fig. 6 Bond strength of HVOF $Ti_{28.15}Al_{63.4}Nb_{8.25}Y$ coatings with different bond coats

3.3 Bond Strength

The bond strength values of HVOF $Ti_{28.15}Al_{63.4}Nb_{8.25}Y$ coatings with different bond coats (NiCr5Al, NiCoCrAlY, CoCrAlYTaSi, and NiCr80/20) are shown in Fig. 6. Among the specimens, HVOF $Ti_{28.15}Al_{63.4}Nb_{8.25}Y$ coatings with the NiCoCrAlY bond coat displayed the highest bond strength. The HVOF $Ti_{28.15}Al_{63.4}Nb_{8.25}Y$ coatings with NiCr5Al bond coat had lower bond strength values than the HVOF $Ti_{28.15}Al_{63.4}Nb_{8.25}Y$ coatings with NiCoCrAlY bond coat. HVOF $Ti_{28.15}Al_{63.4}Nb_{8.25}Y$ coatings with CoCrAlYTaSi bond coat showed the lowest bond strength values.

The bonded rods of all the tested cases failed in the same mode. First, the failure started at the edge of coatings which were sprayed on the flat surface of bonded rods. Then, crack propagated through the coating. Finally, the bonded rods separated through the epoxy glue. To understand where coating failure occurred, EDS analysis of the coating fracture area under area scanning model was applied. The typical fracture surface of NiCr5Al bonded rod (the flat surface of bonded rod sprayed with $Ti_{28.15}Al_{63.4}Nb_{8.25}Y$ top coating and NiCr5Al bond coating) after adhesion test was subjected to SEM inspection. The SEM micrographs and EDS analysis of the fracture surface are shown in Fig. 7 and Table 4, respectively. Among them, SEM micrograph of the fracture surface of bonded rod after adhesion test is shown in Fig. 7(a), and Fig. 7(b) displayed the high-magnification SEM micrograph of coating fracture area in Fig. 7(a). The EDS spectrum and analysis results, as shown in Fig. 7(c) and Table 4 indicated that elements Fe, Ni, Cr, and Al existed in the coating fracture area of sample. Furthermore, the components (Ti and Nb) of HVOF $Ti_{28.15}Al_{63.4}Nb_{8.25}Y$ top coating were not detected. Fe should be from the 316L stainless steel substrate and it showed a typical adhesive failure of HVOF $Ti_{28.15}Al_{63.4}Nb_{8.25}Y$ coatings. Elements Ni, Cr, and Al showed a cohesive failure of the HVOF $Ti_{28.15}Al_{63.4}Nb_{8.25}Y$ coatings and the lack of element Ti and Nb indicated that the crack proceeded within the bond coat. The results showed that a mixed failure mode of adhesive (coating to substrate) and cohesive (within the inter- and intra-lamellar structure of coating) occurred in the tested samples. Due to the thermal mismatch between bond coat and substrate, the micro-cracks are easier to propagate and extend in bond coat (Ref 32).

During the process of spraying, the flight particles were sprayed on the stainless steel substrate and produced the peening stresses between coating and substrate. The mechanism interlock strength of nonspherical particles was higher than that of the spherical ones. Furthermore, the mismatch in thermal expansion coefficients between HVOF NiCoCrAlY bond coating and 316L stainless steel substrate (shown in Table 5) is small; therefore, the cooling stress in thermally sprayed coating with NiCoCrAlY bond coat is lower than the other three bond coats. In addition, as stated in Ref 33, nonspherical particles reached higher average velocities than spherical powder at the same operation parameters due to higher drag coefficient for nonspherical particles; the kinetic energy prior to impact was a key factor for strong adhesion. Moreover, the higher roughness value ($Ra = 6.74$ μm) of HVOF NiCoCrAlY bond coat had a beneficial effect of bond strength. All these would account for the highest bond strength of HVOF NiCoCrAlY coatings.

3.4 Porosity

The porosity values of bond coats (NiCr5Al, NiCoCrAlY, CoCrAlYTaSi, and NiCr80/20) and HVOF $Ti_{28.15}Al_{63.4}Nb_{8.25}Y$ top coats were determined by the image tool analysis, as shown in Fig. 8 and 9. As revealed in Fig. 8, the porosities of bond coats (NiCr5Al, NiCoCrAlY, CoCrAlYTaSi, and NiCr80/20) were 1.22, 1.24, 0.74, and 0.41%, respectively. The results clearly demonstrated that the bond coats of NiCr5Al and NiCoCrAlY had higher

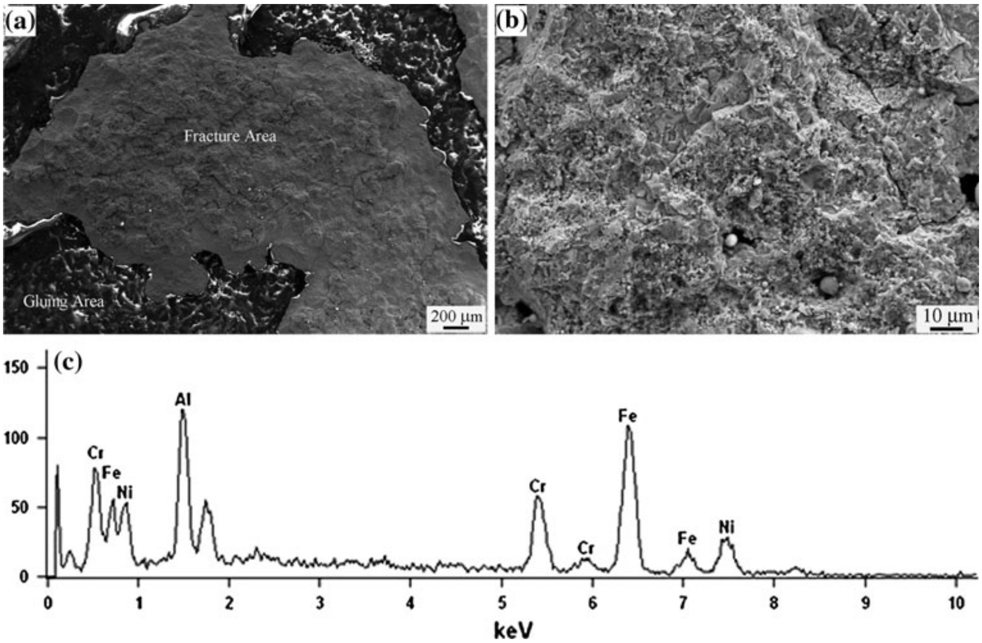

Fig. 7 SEM micrographs and EDS analysis of the fracture surface of bonded rod (the flat surface of bonded rod HVOF sprayed with $Ti_{28.15}Al_{63.4}Nb_{8.25}Y$ top coating and NiCr5Al bond coating) after adhesion test (a) SEM micrograph of the fracture surface of bonded rod after adhesion test (b) high-magnification SEM micrograph of coating fracture area in (a). (c) EDS spectrum of coating fracture area in (a)

Table 4 EDS analysis results of the spectrum shown in Fig. 7(c)

Element line	Weight %	Weight % error	Atom %	Atom % error
Al K	14.27	±0.43	25.56	±0.77
Cr K	16.58	±0.60	15.41	±0.56
Fe K	49.46	±1.22	42.81	±1.05
Ni K	19.7	±1.06	16.22	±0.87

porosity values than the CoCrAlYTaSi and NiCr80/20 bond coats. Porosity was lower in the bond coats (CoCrAlYTaSi and NiCr80/20) which were deposited using the spherical feedstock powders. It was probably because of their more regular shape and narrower size distribution, as shown in Table 1. During the process of HVOF spraying, regular shape and narrower size distribution of spray powder resulted in more homogeneous heating and acceleration and reduced the formation of defects. Furthermore, the curved surface of the spherical particle permits the kinetic energy to flow from the nearby nodes and increases the internal energy of spherical particles.

On the other hand, it is seen in Table 1 that the nonspherical particles possess much broader particle size distribution than the spherical ones. Particles with very different sizes cannot be uniformly treated in the HVOF jet; therefore, the broad particle size distribution is likely to result in greater inhomogeneity, larger defectiveness and higher porosity in the coating. Excessively fine particles are overheated and severely oxidized (especially in an oxidizing, oxygen-rich flame), while large ones are unmelted, producing nonflattened inclusions.

Furthermore, increased contacting area between the nonspherical particles and lower temperature profiles induce the lower levels of plastic deformation. So, the spherical powder gives denser coating, whereas the milled nonspherical powder creates more porous coatings (Ref 32).

The porosity values of HVOF $Ti_{28.15}Al_{63.4}Nb_{8.25}Y$ top coatings with different bond coats (NiCr5Al, NiCoCrAlY, CoCrAlYTaSi, and NiCr80/20) are displayed in Fig. 9. The results clearly demonstrated that the HVOF $Ti_{28.15}Al_{63.4}Nb_{8.25}Y$ top coatings with different bond coats had the close porosity values. In general, small particles are favorable to forming dense coatings after thermal spraying. As shown in Table 1, the particle size of $Ti_{28.15}Al_{63.4}Nb_{8.25}Y$ was smaller. During the process of HVOF spraying, the smaller the particle size, the more easily it is to be accelerated and decelerated. After HVOF spray, the higher levels of plastic deformation of smaller particles give denser coatings. HVOF $Ti_{28.15}Al_{63.4}Nb_{8.25}Y$ top coatings with different bond coats (NiCr5Al, NiCoCrAlY, CoCrAlYTaSi, and NiCr80/20) had close porosity values at the same operation conditions. The bond coats had slight effects on the porosity of HVOF $Ti_{28.15}Al_{63.4}Nb_{8.25}Y$ top coatings.

3.5 Microhardness

Hardness is the most frequently quoted mechanical property of the coatings. The Vickers hardness values ($HV_{0.1}$) along the cross section of HVOF $Ti_{28.15}Al_{63.4}$

Table 5 Thermal expansion coefficient of coating materials

Alloys	$Ti_{28.15}Al_{63.4}$ $Nb_{8.25}Y$	316L Stainless Steel	NiCr	CoCrAlYTaSi	NiCoCrAlY	NiCr5Al
Temperature, °C	825	825	825	825	825	825
Thermal expansion coefficient (10^{-6}/K)	13.01	17.9	13.42	13.48	13.84	13.62

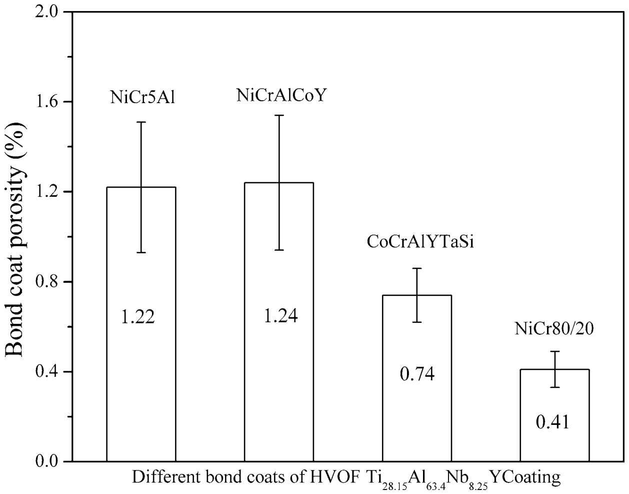

Fig. 8 Porosity values of NiCr5Al, NiCoCrAlY, CoCrAlYTaSi, and NiCr80/20 bond coats of HVOF $Ti_{28.15}Al_{63.4}Nb_{8.25}Y$ coatings

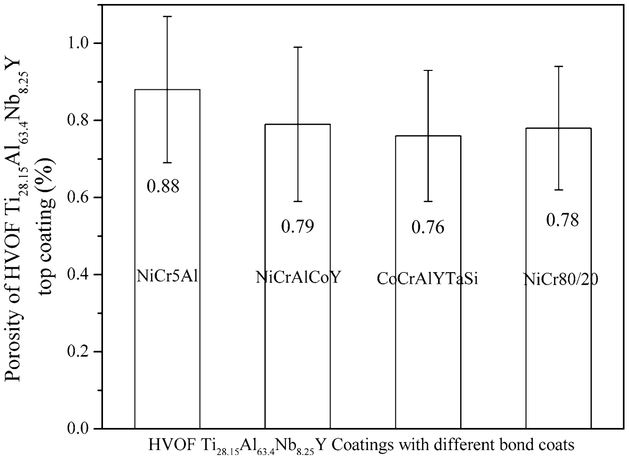

Fig. 9 Porosity values of HVOF $Ti_{28.15}Al_{63.4}Nb_{8.25}Y$ top coats with NiCr5Al, NiCoCrAlY, CoCrAlYTaSi, and NiCr80/20 bond coat

$Nb_{8.25}Y$ coatings deposited on 316L stainless steel substrate with different bond coats (NiCr5Al, NiCoCrAlY, CoCrAlYTaSi, and NiCr80/20) are shown in Fig. 10. The measured hardness values for each bond coat were 282.5-362.3 for NiCr5Al bond coat, 335.1-396.2 for NiCoCrAlY bond coat, 684.5-725.3 for CoCrAlYTaSi bond coat, and 321.4-374.6 for NiCr80/20 bond coat.

Among the four kinds of bond coats, CoCrAlYTaSi displayed the highest microhardness values. The hardness values of the HVOF $Ti_{28.15}Al_{63.4}Nb_{8.25}Y$ top coatings with

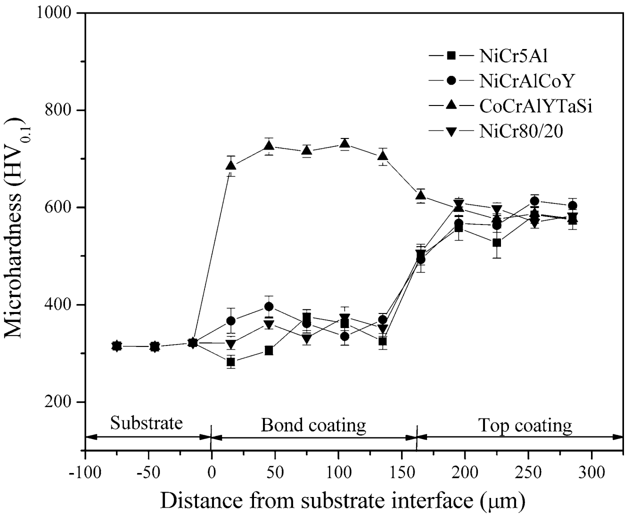

Fig. 10 Microhardness values of HVOF $Ti_{28.15}Al_{63.4}Nb_{8.25}Y$ coatings deposited on 316L stainless steel substrate with NiCr5Al, NiCoCrAlY, CoCrAlYTaSi, and NiCr80/20 bond coats

different bond coats lay in the range of 500-600. The hardness values of the HVOF $Ti_{28.15}Al_{63.4}Nb_{8.25}Y$ top coatings were significantly higher than that of the 316L stainless steel substrate. The nonuniformity of the hardness values of HVOF $Ti_{28.15}Al_{63.4}Nb_{8.25}Y$ top coatings was probably attributed to the microstructural changes along the cross section of the coatings (Ref 34). These microstructural changes might be due to the presence of porosity, oxidized, melted, unmelted, and semi-melted particles in the coating structure as observed in SEM and optical micrographs (Ref 35, 36). Porosity in coating has a negative effective on the hardness of coatings. Excessive porosities in the coatings will cause the falling of hardness values (Ref 37).

3.6 Thermal Shock Test

Optical photograph of spalled sample after thermal shock test is shown in Fig. 11. Figure 12 gives the results of thermal shock test of the HVOF $Ti_{28.15}Al_{63.4}Nb_{8.25}Y$ coatings with different bond coats (NiCr5Al, NiCoCrAlY, CoCrAlYTaSi, and NiCr80/20). The results indicated that the HVOF $Ti_{28.15}Al_{63.4}Nb_{8.25}Y$ coating with NiCoCrAlY bond coat displayed the best thermal shock life. On the contrary, the HVOF $Ti_{28.15}Al_{63.4}Nb_{8.25}Y$ coating with CoCrAlYTaSi bond coat revealed the worst thermal shock life. The cycling number of the coating with NiCoCrAlY bond coat reached 116 in thermal shock test. But,

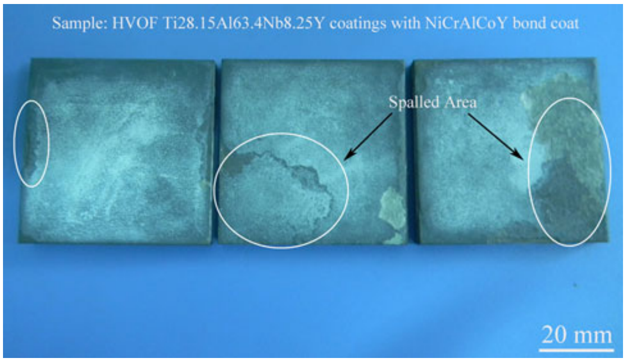

Fig. 11 Optical photograph of spalled samples of HVOF $Ti_{28.15}Al_{63.4}Nb_{8.25}Y$ coatings with NiCoCrAlY bond coats after thermal shock test

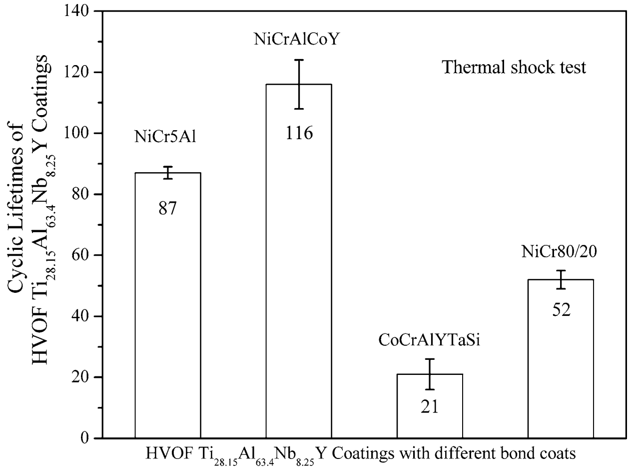

Fig. 12 Cycling number of HVOF $Ti_{28.15}Al_{63.4}Nb_{8.25}Y$ coatings with NiCr5Al, NiCoCrAlY, CoCrAlYTaSi, and NiCr80/20 bond coats in thermal shock tests

the coat with CoCrAlYTaSi bond coat failed after 21 thermal cyclings at 600 °C.

All the samples of the HVOF $Ti_{28.15}Al_{63.4}Nb_{8.25}Y$ coatings with different bond coats (NiCr5Al, NiCoCrAlY, CoCrAlYTaSi, and NiCr80/20) failed along the interface between the bond coat and substrate, rather than along the interface between the top coat and the bond coat or in the HVOF $Ti_{28.15}Al_{63.4}Nb_{8.25}Y$ top coating.

During the process of thermal shock testing, there was no macro-crack in the coating samples (HVOF $Ti_{28.15}Al_{63.4}Nb_{8.25}Y$ coating with NiCr5Al, NiCoCrAlY, CoCrAlYTaSi, and NiCr80/20 bond coat, respectively) after 15 thermal cyclings. However, after 18 thermal cyclings, the edge of HVOF $Ti_{28.15}Al_{63.4}Nb_{8.25}Y$ coating with CoCrAlYTaSi bond coat started to spall and drop first due to the shearing stress. The micro-crack propagated and extended gradually in the coatings near the edge with the increase of thermal cyclings. The cracks increased and some appeared to close while they form an obvious network state. Furthermore, the coatings of HVOF $Ti_{28.15}Al_{63.4}Nb_{8.25}Y$ coating with CoCrAlYTaSi bond coat dropped in large pieces after 21 thermal cyclings. Spallation with more than 20% of the total area of the coating was adopted as the criteria for coating failure.

The failure modes of the HVOF $Ti_{28.15}Al_{63.4}Nb_{8.25}Y$ coatings with different bond coats (NiCr5Al, NiCoCrAlY, CoCrAlYTaSi, and NiCr80/20) in thermal shock testing were the same. The failure mode was as follows. To begin with, due to the shearing stress, the edge of all the tested samples started to spall and drop first. Second, the micro-crack propagated and expanded in the nearby coatings. Finally, the coatings dropped in large pieces at the end of thermal shock testing. However, the thermal cycles of HVOF $Ti_{28.15}Al_{63.4}Nb_{8.25}Y$ coatings with different bond coats (NiCr5Al, NiCoCrAlY, CoCrAlYTaSi, and NiCr80/20) began to peel off are different. They are 78, 90, 18, and 47, respectively.

The bond strength and thermal stress of sprayed coatings should be considered as significant influence factors on thermal shock property. High bond strength is conducive to better thermal shock property of coatings for a longer lifetime. Except for the cooling and peening stresses existed in the coatings which were stated in section 3.3, the quenching stresses also play an important role on the thermal cyclic behavior of coatings. The thermal shock test was performed by water quenching method and would induce stress concentration in the interface between bond coat and substrate due to the thermal expansion mismatch. The smaller the thermal expansion mismatch is, the smaller the stress concentration will be. The HVOF $Ti_{28.15}Al_{63.4}Nb_{8.25}Y$ coating with NiCoCrAlY bond coat exhibited great thermal shock property, resulting from the summation of all these contributions. However, the HVOF $Ti_{28.15}Al_{63.4}Nb_{8.25}Y$ coating with CoCrAlYTaSi bond coat displayed the smallest cyclic lifetime in thermal shock test. Except for the low bond strength of HVOF $Ti_{28.15}Al_{63.4}Nb_{8.25}Y$ coating with CoCrAlYTaSi bond coat as stated in th above, the higher residual stress in HVOF $Ti_{28.15}Al_{63.4}Nb_{8.25}Y$ coating was an another important influence factor accounted for the smallest cyclic lifetime in thermal shock test. The large difference of coefficient of thermal expansion (CTE) between CoCrAlYTaSi bond coat and 316L stainless steel substrate would induce higher residual stress and result in the cracking and spalling of HVOF $Ti_{28.15}Al_{63.4}Nb_{8.25}Y$ coating. The thermal stress was simulated below.

For the coating-substrate system, adhesion is one of the most important properties. However, the mismatch of CTE between the substrate and the top coating would generate residual stresses in the coating or at interface of the coating and substrate, which would result in bending, microcracking, spalling, and even delamination phenomena (Ref 38).

Applying an appropriate intermediate bond coating between top coating and substrate is an effective way to improve the bonding property of coating with substrate. In the previous work, the bond strength values of HVOF TiAlNb coatings with bond coats were higher than that of monolayer TiAlNb coating. In addition, the lifetime of HVOF $Ti_4Nb_3Al_9$ coatings with NiCr5Al bond coat (substrate: 410 stainless steel) in molten Zn-0.2 wt.% Al reached 45 days. But, the lifetime of HVOF $Ti_4Nb_3Al_9$

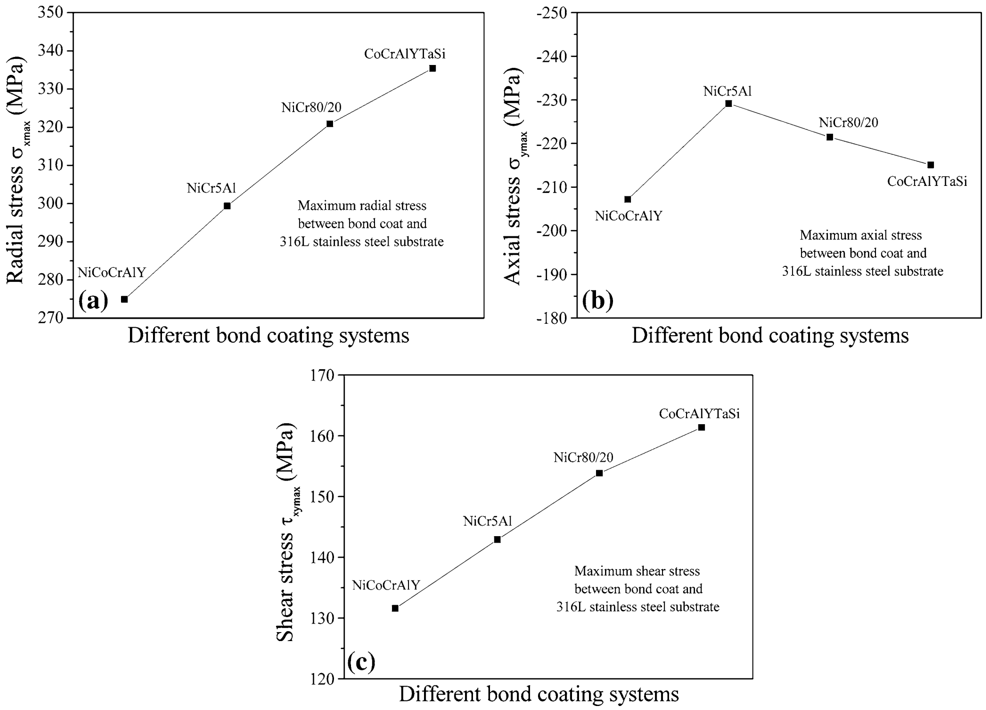

Fig. 13 Radial stress, axial stress, and shear stress of HVOF $Ti_{28.15}Al_{63.4}Nb_{8.25}Y$ coatings between different bond coats (NiCr5Al, NiCoCrAlY, CoCrAlYTaSi, and NiCr80/20) and 316L stainless steel substrate. (a) Radial stress, (b) axial stress, and (c) shear stress

monolayer coatings in molten Zn-0.2 wt.% Al were only 30 h due to the mismatch of CTE between the substrate and the HVOF $Ti_4Nb_3Al_9$ top coating. Bond coating layer provided a good transition of CTE between substrate and top coating.

The effects of bond coat on the top coat were mainly concentrated on the mechanical properties such as bond strength and thermal shock resistance. Bond coat had no effects on the phase composition of top coating. The phase composition of top coating is up to the parameter of spraying. In addition, the bond coat affects the microhardness, porosity, and microstructure of the whole coating (bond coat and top coat).

To evaluate the thermal stress of HVOF $Ti_{28.15}Al_{63.4}Nb_{8.25}Y$ coatings with different bond coats (NiCr5Al, NiCoCrAlY, CoCrAlYTaSi, and NiCr80/20) between bond coat and 316L stainless steel substrate, ANSYS software (ANSYS Corporation, Canonsburg, PA) was used to simulate the radial stress, axial stress, and shear stress of HVOF $Ti_{28.15}Al_{63.4}Nb_{8.25}Y$ coatings induced by the CTE mismatch between bond coat and 316L stainless steel substrate. The simulated reference temperature was 600 °C. The thermal stress of HVOF $Ti_{28.15}Al_{63.4}Nb_{8.25}Y$ coatings is the residual stress which was induced by the cooling of HVOF $Ti_{28.15}Al_{63.4}Nb_{8.25}Y$ coatings from 600 to 25 °C.

The radial stress, axial stress, and shear stress of HVOF $Ti_{28.15}Al_{63.4}Nb_{8.25}Y$ coatings are shown in Fig. 13.

As revealed in Fig. 13, the radial stress, axial stress, and shear stress of HVOF $Ti_{28.15}Al_{63.4}Nb_{8.25}Y$ coatings between NiCoCrAlY bond coat and 316L stainless steel substrate were the lowest in the four kinds HVOF $Ti_{28.15}Al_{63.4}Nb_{8.25}Y$ coatings with different bond coats (NiCr5Al, NiCoCrAlY, CoCrAlYTaSi, and NiCr80/20). The radial stress, axial stress, and shear stress were 274.9, −207.1, and 131.6 MPa, respectively. Compared with NiCoCrAlY bond coat, the radial stress, axial stress, and shear stress between NiCr5Al bond coat and 316L stainless steel substrate were higher. Among the four bond coatings (NiCr5Al, NiCoCrAlY, CoCrAlYTaSi, and NiCr80/20), the radial stress and shear stress between CoCrAlYTaSi bond coat and 316L stainless steel substrate were the highest. The residual stress in coatings has an obviously influences on the mechanical properties and service life of coatings. The residual stress in coatings will be higher due to the bigger values of CTE mismatch between bond coat and substrate and which will induce the reduction of coating lifetimes. The simulation result was consistent with the findings of testing.

4. Conclusions

In this study, HVOF $Ti_{28.15}Al_{63.4}Nb_{8.25}Y$ coatings with four different bond coats (NiCr5Al, NiCoCrAlY, CoCrAlYTaSi, and NiCr80/20) were compared. The effects of bond coat on the properties of HVOF $Ti_{28.15}Al_{63.4}Nb_{8.25}Y$ top coating such as microstructure, porosity, hardness, and thermal shock performance were investigated. The investigation has shown that the mechanical properties (bond strength and thermal shock resistance) of HVOF $Ti_{28.15}Al_{63.4}Nb_{8.25}Y$ coatings can be improved significantly by applying bond coats. The HVOF $Ti_{28.15}Al_{63.4}Nb_{8.25}Y$

coating with NiCoCrAlY bond coat displayed the highest bond strength value of 51.3 MPa and showed the best thermal shock performance. Bond coat had no effects on the phase composition of HVOF $Ti_{28.15}Al_{63.4}Nb_{8.25}Y$ top coating and the high cooling rate induced the formation of $AlTi_3$ metastable phase in HVOF $Ti_{28.15}Al_{63.4}Nb_{8.25}Y$ top coating. The microstructure, porosity, and hardness of HVOF $Ti_{28.15}Al_{63.4}Nb_{8.25}Y$ top coating were not influenced obviously by different bond coats. Furthermore, smaller particle size and spherical powders preferred to give denser and uniform microstructure of spray coatings. The bond coat material of NiCoCrAlY was the most suitable for HVOF $Ti_{28.15}Al_{63.4}Nb_{8.25}Y$ top coating for finer mechanical properties.

Acknowledgments

The authors wish to acknowledge the financial support received from the National Key Basic Research Program of China (973 Program, No. 2011CB605502, the National Natural Science Foundation of China under Contract No. 50871127 and the State Key Laboratory for Advanced Metals and Materials, University of Science and Technology Beijing, under contract No. 2008Z-05, as well as D.W. An for his assistance with the thermal spraying equipment.

References

1. S.M.A. Shibli, R. Manu, and S. Beegum, Studies on the Influence of Metal Oxides on the Galvanic Characteristics of Hot-Dip Zinc Coating, *Surf. Coat. Technol.*, 2008, **202**, p 1733-1737
2. S.K. Chuchmarev, V.I. Pokhmurskii, Yu.A. Raevskii, Yu.G. Dmitriev, and O.Ya Lizun, Kinetics of Solution of Iron in Molten Zinc, *J. Mater. Sci.*, 1985, **21**, p 411-413
3. S.M.A. Shibli and R. Manu, Improvement of Hot-Dip Zinc Coating by Enriching the Inner Layers with Iron Oxide, *Appl. Surf. Sci.*, 2006, **252**, p 3058-3064
4. S.M.A. Shibli, R. Manu, and V.S. Dilimon, Effect of Nickel-Rich Barrier Layer on Improvement of Hot-Dip Zinc Coating, *Appl. Surf. Sci.*, 2005, **245**, p 179-185
5. Z.A. Hamid, A.A. Aal, H.B. Hassan, and A. Shaaban, Process and Performance of Hot Dip Zinc Coatings Containing ZnO and Ni-P Under Layers as Barrier Protection, *Appl. Surf. Sci.*, 2010, **256**, p 4166-4170
6. Y.C. Dong, D.R. Yan, J.N. He, J.X. Zhang, and X.Z. Li, Degradation Behaviour of ZrO_2-Ni/Al Gradient Coatings in Molten Zn, *Surf. Coat. Technol.*, 2006, **201**, p 2455-2459
7. W.J. Wang, J.P. Lin, Y.L. Wang, Y. Zhang, and G.L. Chen, Isothermal Corrosion TiAl-Nb Alloy in Liquid Zinc, *Mater. Sci. Eng. A*, 2007, **452**, p 194-201
8. A. Scrivani, U. Bardi, L. Carrafiello, A. Lavacchi, F. Niccolai, and G. Rizzi, A Comparative Study of High Velocity Oxygen Fuel, Vacuum Plasma Spray, and Axial Plasma Spray for the Deposition of CoNiCrAlY Bond Coat Alloy, *J. Therm. Spray Technol.*, 2003, **12**, p 504-507
9. H. Waki, T. Kitamura, and A. Kobayashi, Effect of Thermal Treatment on High-Temperature Mechanical Properties Enhancement in LPPS, HVOF, and APS CoNiCrAlY Coatings, *J. Therm. Spray Technol.*, 2009, **18**, p 500-509
10. F.-L. Toma, C.C. Stahr, L.-M. Berger, S. Saaro, M. Hermann, D. Deska, and G. Michael, Corrosion Resistance of APS- and HVOF Sprayed Coatings in the Al_2O_3-TiO_2 System, *J. Therm. Spray Technol.*, 2010, **19**, p 137-147
11. M.P. Planche, H. Liao, B. Normand, and C. Coddet, Relationships Between NiCrBSi Particle Characteristics and Corresponding Coating Properties Using Different Thermal Spraying Processes, *Surf. Coat. Technol.*, 2005, **200**, p 2465-2473
12. S. Deshpande, S. Sampath, and H. Zhang, Mechanisms of Oxidation and Its Role in Microstructural Evolution of Metallic Thermal Spray Coatings—Case Study for Ni-Al, *Surf. Coat. Technol.*, 2006, **200**, p 5395-5406
13. S. Sharma, Erosive Wear Study of Rare Earth-Modified HVOF-Sprayed Coatings Using Design of Experiment, *J. Therm. Spray Technol.*, 2012, **21**, p 49-62
14. B.G. Seong, S.Y. Hwang, M.C. Kim, and K.Y. Kim, Reaction of WC-Co Coating with Molten Zinc in a Zinc Pot of a Continuous Galvanizing Line, *Surf. Coat. Technol.*, 2001, **138**, p 101-110
15. H. Mizuno and J. Kitamura, MoB/CoCr Cermet Coatings by HVOF Spraying against Erosion by Molten Al-Zn Alloy, *J. Therm. Spray Technol.*, 2007, **16**, p 404-413
16. B.G. Seong, S.Y. Hwang, M.C. Kim, K.Y. Kim, Observation on the WC-Co Coating Used in a Zinc Pot of a Continuous Galvanizing Line, Thermal Spray: Surface Engineering Via Applied Research, C.C. Berndt, Ed., May 8-11, 2000 (Canada), ASM International, Materials Park, OH, USA, 2000, p 1159-1167
17. W.J. Wang, J.P. Lin, Y.L. Wang, and G.L. Chen, The Corrosion of Intermetallic Alloys in Liquid Zinc, *J. Alloys Compd.*, 2007, **428**, p 237-243
18. J.-Y. Kwon, J.-H. Lee, H.-C. Kim, Y.-G. Jung, U. Paik, and K.-S. Lee, Effect of Thermal Fatigue on Mechanical Characteristics and Contact Damage of Zirconia-Based Thermal Barrier Coatings with HVOF-Sprayed Bond Coat, *Mater. Sci. Eng. A*, 2006, **429**, p 173-180
19. P.K. Wright and A.G. Evans, Mechanisms Governing the Performance of Thermal Barrier Coatings, *Curr. Opin. Solid State Mater. Sci.*, 1999, **4**, p 255-265
20. A. Fossati, M. DiFerdinando, U. Bardi, A. Scrivani, and C. Giolli, Influence of Surface Finishing on the Oxidation Behaviour of VPS MCrAlY Coatings, *J. Therm. Spray Technol.*, 2012, **21**, p 314-324
21. A. Atkinson, A. Selcuk, and S.J. Webb, Variability of Stress in Alumina Corrosion Layers Formed in Thermal-Barrier Coatings, *Oxid. Met.*, 2000, **54**, p 371-384
22. B.A. Pint, I.G. Wright, W.Y. Lee, Y. Zhang, and K.B. Alexander, Substrate and Bond Coat Compositions: Factors Affecting Alumina Scale Adhesion, *Mater. Sci. Eng. A*, 1998, **245**, p 201-211
23. H.P. Lu, P.L. Nie, Y.G. Yan, J. Wang, and B.D. Sun, Microstructure and Interfacial Adhesion of High Velocity Oxy-Fuel-Sprayed MoB-CoCr Alloy Coating on 316L Stainless Steel, *Surf. Interface Anal.*, 2009, **41**, p 725-729
24. S. Matthews and B. James, Review of Thermal Spray Coating Applications in the Steel Industry: Part 2—Zinc Pot Hardware in the Continuous Galvanizing Line, *J. Therm. Spray Technol.*, 2010, **19**, p 1277-1286
25. J.P. Lin, W.J. Wang, Y.L. Wang, Y. Zhang, Z. Lin, G.L. Chen, An Intermetallic Compound-TiAlNb of Corrosion Resistance to Molten Zinc, China Patent, Publication Number CHN 10011237. 5, Beijing University of Technology, 2006 (in Chinese)
26. P.F. Sun, L.Q. Zhang, L. Zhang, and J.P. Lin, Improvement in the Liquid Zinc Corrosion Resistance of High Nb-TiAl Alloys by Pre-oxidation in a SiO_2-Powder Pack, *Sci. China E*, 2012, **55**, p 505-509
27. H.J. Zeng, L.Q. Zhang, J.P. Lin, S.J. Zhang, and G.L. Chen, TiAlNb Intermetallic Compound Coating Prepared by High Velocity Oxy-Fuel Spraying, *Surf. Coat. Technol.*, 2011, **206**, p 178-184
28. "Standard Test Method for Adhesion or Cohesion Strength of Thermal Spray Coatings," C 633-01, Annual Book of ASTM Standards, ASTM, 2001, **3**, p 1-7
29. X.G. Sun, S.F. Chen, Y. Wang, Z.Y. Pan, L. Wang, Mechanical Properties and Thermal Shock Resistance of HVOF Sprayed NiCrAlY Coatings Without and With Nano Ceria, *J. Therm. Spray Technol.*, 2012, **21**, p 818-824
30. P. Richer, M. Yandouzi, L. Beauvais, and B. Jodoin, Oxidation Behaviour of CoNiCrAlY Bond Coats Produced by Plasma, HVOF, and Cold Gas Dynamic Spraying, *Surf. Coat. Technol.*, 2010, **204**, p 3962-3974

31. K. Fritscher, Eutectic Structures in the Ni-Co-Cr-Al System Obtained by Plasma Spraying and by Bridgman Growth, *Cryst. Growth*, 2003, **250**, p 546-557
32. H.D. Steffens, B. Wielage, and J. Drozak, Interface Phenomena and Bonding Mechanism of Thermally-Sprayed Metal and Ceramic Composites, *Surf. Coat. Technol.*, 1991, **45**, p 299-308
33. S. Kamnis and S. Gu, Study of In-Flight and Impact Dynamic of Nonspherical Particles from HVOF Guns, *J. Therm Spay. Technol.*, 2010, **19**, p 31-41
34. R.A. Mahesh, R. Jayaganthan, and S. Prakash, Microstructural Characterization and Hardness Evaluation of HVOF Sprayed Ni-5Al Coatings on Ni- and Fe-Based Superalloys, *J. Mater. Process. Technol.*, 2009, **209**, p 3501-3510
35. B.S. Sidhu, D. Puri, and S. Prakash, Mechanical and Metallurgical Properties of Plasma Sprayed and Laser Remelted Ni-20Cr and Stellite-6 Coatings, *J. Mater. Process. Technol.*, 2005, **159**, p 347-355
36. H.S. Sidhu, B.S. Sidhu, and S. Prakash, Mechanical and Microstructural Properties of HVOF Sprayed WC-Co and Cr_3C_2-NiCr Coatings on the Boiler Tube Steels Using LPG as the Fuel Gas, *J. Mater. Process. Technol.*, 2006, **171**, p 77-82
37. F.F. Khan, G. Bae, K. Kang, N. Hyuntaek, J. Kim, T. Jeong, and C. Lee, Evaluation of Die-Soldering and Erosion Resistance of High Velocity Oxy-Fuel Sprayed MoB-Based Cermet Coatings, *J. Therm. Spray Technol.*, 2011, **20**, p 1022-1034
38. Y.R. Niu, D.Y. Hu, H. Ji, L.P. Huang, and X.B. Zheng, Effect of Bond Coatings on Properties of Vacuum Plasma Sprayed Tungsten Coatings on Copper Alloy Substrate, *Fusion Eng. Des.*, 2011, **86**, p 307-311